J Solid State Electrochem (2017) 21:975–985
DOI 10.1007/s10008-016-3439-5

ORIGINAL PAPER

Effect of carbonaceous support between graphite oxide and reduced graphene oxide with anchored Co_3O_4 microspheres as electrode-active materials in a solid-state electrochemical capacitor

V. Parra-Elizondo[1] · B. Escobar-Morales[1] · E. Morales[2] · D. Pacheco-Catalán[1]

Received: 22 June 2016 / Revised: 9 October 2016 / Accepted: 14 October 2016 / Published online: 2 November 2016

Abstract Hydrothermally synthesized Co_3O_4 microspheres were anchored to graphite oxide (GO) and thermally reduced graphene oxide (rGO) composites at different cobalt weight percentages (1, 10, and 100 wt%). The composite materials served as the active materials in bulk electrodes for two-electrode cell electrochemical capacitors (ECCs). GO/Co_3O_4–1 exhibited a high energy density of 35 W kg^{-1} with a specific capacitance (C_{sp}) of 196 F g^{-1} at a maximum charge density of 1 A g^{-1}. rGO/Co_3O_4-100 presented high specific power output values of up to 23.41 kW h kg^{-1} with linear energy density behavior for the charge densities applied between 0.03 and 1 A g^{-1}. The composite materials showed Coulombic efficiencies of 96 and 93 % for GO/Co_3O_4–1 and rGO/Co_3O_4–100 respectively. The enhancement of capacitive performance is attributed to the oxygenated groups in the GO ECC and the specific area in the rGO ECC. These results offer an interesting insight into the type of carbonaceous support used for graphene derivative electrode materials in ECCs together with Co_3O_4 loading to improve capacitance performance in terms of specific energy density and specific power.

Keywords Energy storage · Graphite oxide · Reduced graphene oxide · Co_3O_4 · Electrochemical capacitor · Hydrothermal synthesis

Introduction

Maintaining the energy supply is an important issue for industry and urban development in the present day. In order to deal with this problem, it is essential to transition to clean renewable energy sources as fossil fuels become more depleted, as well as due to the environmental problems associated with greenhouse gas emissions. For this transition to be successful, better renewable energy production, usage, and storage are needed. As such, energy storage technologies play an important role in the transition to renewable energy. Electrochemical energy storage technologies are able to collect and deliver a constant power supply through chemical or physical processes involving the transfer of electrons between electrode materials. Among the existing types of energy storage devices, electrochemical capacitors (ECCs) offer several operational advantages to complement other energy storage devices such as batteries [1, 2]. Their most remarkable advantages include high specific power output, low charge/discharge time rates, no maintenance, and cyclability one thousand times greater than batteries, making ECCs a promising energy storage technology [3]. The energy storage mechanism in an ECC is based on two processes. The first mechanism stores energy through a coupled system of processes involving the adsorption-desorption of ion species along the electrode-electrolyte interface in the electrochemical double layer (ECDL) across the surface area of the electrode. This process is highly reversible because it only involves the transfer of charge between electrodes and there are no chemical reactions involved [4]. The second energy storage mechanism in an ECC is through faradaic contributions produced by the

Electronic supplementary material The online version of this article (doi:10.1007/s10008-016-3439-5) contains supplementary material, which is available to authorized users.

✉ D. Pacheco-Catalán
dpacheco@cicy.mx

[1] Centro de Investigación Científica de Yucatán, Carretera Sierra Papacal – Chuburná Puerto, km 5. Sierra Papacal, Mérida C.P. 97302, Yucatán, Mexico

[2] Instituto de Ciencia y Tecnología de Polímeros, C/ Juan de la Cierva 3, 28006 Madrid, Spain

redox process in electrode-active materials. These Faradaic contributions increase the charge density and are limited by the reversibility of the materials involved in the redox process [5]. Carbon materials are widely used as building blocks for electrodes in ECCs. Properties such as high chemical and thermal stability, high cycling capability and large specific area for the accumulation of charge make carbon materials an excellent base for storing charge energy via the ECDL mechanism [6, 7]. Although energy density is a limiting factor for ECCs based on carbonaceous materials, numerous reports have evaluated the electrochemical proprieties of Co_3O_4. Given its electrochemical stability, tunable morphology and the versatility of its preparation methods, Co_3O_4 is a good candidate for use in energy storage applications. Recent advances in ECC studies have used composites with metal oxides as the active material on different types of carbon supports, such as graphene oxide [8], carbon nanotubes [9], and activated carbon [10], as well as using cobalt nitrides as a faradaic promoter in hybrid ECC (HECC) arrangements through urea combustion to ensure nanometric particle size [11]. Other reported strategies use binary or ternary metal oxides in a composite electrode, taking advantage of the structural diversity of the metal oxides to enhance capacity [12], as well as using phosphate and pyrophosphate metal complexes as intercalation compounds to host Li ions in non-aqueous electrolytes in HECC electrodes [13].

Hydrothermal synthesis offers an easy and controllable synthesis technique for metal oxide composites for ECC electrode materials [14–17]. Different morphologies have been reported including rugby ball-like structures of Co_3O_4 with high cycling properties of over 10,000 charge/discharge cycles with energy density values of 14.3 W h kg^{-1} and a power density of 7.5 kW kg^{-1} [18]. Co_3O_4 nanoplates over graphene nanosheets had a capacitance loss of 18.7 % after 1000 cycles when tested in a three-electrode cell arrangement [16]. Along with morphology, the percentage of metal oxides has been evaluated. At high weight proportions, Co_3O_4 composites exhibit rapid decomposition after cycling, giving rise to an anomalous increase in the calculated capacitance [19]. However, the use of indistinct nomenclature in graphene derivative carbonaceous materials as supports for the metal oxide in electrode-active materials [20] and electrochemical evaluation in three-electrode-type cells may lead to unclear conclusions for assessment in a more realistic application approach when intended for ECC use. The aim of this work was therefore to use a two-cell ECC to electrochemically evaluate the performance of a series of composite materials synthesized through a hydrothermal process employing two different carbonaceous supports: thermally reduced graphene oxide (rGO) and chemically exfoliated graphene oxide (GO), and varying the Co_3O_4 composition in the composite electrode-active material. Morphology, phase identification, Raman spectroscopic characterization, thermal decomposition, and textural proprieties of the composites were investigated.

Experimental

All chemical reagents were of analytical grade (from Sigma-Aldrich) and were used without further purification. All aqueous solutions were prepared using deionized water.

Synthesis of GO/rGO-Co composites

GO was obtained using the Brodie modification method [21]. In a typical oxidation process, 5 g of graphite with a mesh of 300 were mixed with fuming HNO_3 at 0 °C, and then 14 g of $KClO_3$ were added to the reaction flask. The reaction was kept under agitation for 24 h in an ice bath to avoid the formation of gas by the oxidation process. The resulting yellow material obtained was decanted, filtered, and washed until the pH was neutral. The resulting yellowish-brown material was dried at 80 °C. To obtain rGO, the GO was thermally reduced in a tubular furnace under Ar atmosphere at 250 °C for 1 h. The GO and thermally reduced rGO materials obtained through the oxidation process were used as supports for Co^{2+} from $Co(NO_3)_2{\cdot}6H_2O$ coupled by a hydrothermal process carried out in a Teflon® reactor with a volume of 120 mL.

The composite material was prepared in three different concentrations of Co^{2+} from $Co(NO_3)_2{\cdot}6H_2O$ of 1, 10 and 100 wt% for the GO-based composite and the rGO-based composite respectively, and 6 mL of 0.01 M NaOH was used in each synthesis. The reagents were previously dispersed by sonication for 20 min. Then, the heterogeneous mixture was placed in the Teflon® reactor, sealed, and heated to 160 °C for 24 h with continuous magnetic stirring. The resulting black powder was washed with deionized water, filtered, and dried at 80 °C for 24 h.

Characterization of composite materials

The phases of the composite materials were identified using X-ray powder diffraction (XRD, D8 X Bruker) with Cu Kα irradiation. The scan data were collected in the 2θ range of 10–60° at 2θ/min. The particle morphology of the composite materials was observed by scanning electron microscopy (SEM; HR-Hitachi S-8000) with field emission filament. The thermal stability of the composite materials was evaluated by thermal gravimetric analysis (TGA; TA-Q500 TA Instruments) using an air atmosphere with a heating rate of 5 °C/min. To investigate the hybridization of sp2 and sp3 carbon atoms in the supports, Raman spectroscopy was performed using a Renishaw Raman microscope with a monochromatic light source of 514.5 nm.

Electrode preparation

The electrochemical performance of the composites was analyzed in symmetric two-electrode Swagelok®-type cells.

Supercapacitor electrodes were processed as cylindrical pellets 12 mm in diameter by cold-pressing (200 kg cm^{-2}, 10 min). The electrodes were made by mixing 80 wt% of the composite as the active material (50 mg), 10 wt% of PTFE binder (Aldrich), and 10 wt% of carbon black (SuperP, 3 M). The ECCs were assembled using two electrodes with Whatman 934AH separator in between them and soaked with aqueous 6 M KOH solution as electrolyte. Two stainless steel rods (alloy A20) acted as current collectors. All cells were fully discharged before each experiment.

Electrochemical characterization

Cyclic voltammetry (CV), galvanostatic charge/discharge (GCD), and electrochemical impedance spectroscopy (EIS) electrochemical characterization techniques were used to study the capacitive performance of the composite materials in symmetric two-electrode Swagelok®-type cells using a Solartron 1480 MultiStat potentiostat. Potentiostatic electrochemical impedance spectroscopy (PEIS) was carried out with a coupled Solartron 1255B frequency response analyzer module over a frequency range of 300 kHz to 0.010 Hz with a sinus amplitude of 10 mV against open circuit potential (OCP). CV was measured within a potential window of 0–1 V at a scan rate range of 1–100 mV s^{-1}. GCD measurements were conducted at current densities from 0.03 to 1 A g^{-1} with potential window limits between 0 and 1 V. The capacitance was obtained by different electrochemical techniques. Specific capacitance obtained by CV is given by Eq. 1 [22]:

$$C_{\mathrm{sp}} = \frac{A}{U \times v \times m_{\mathrm{electrode}}} \tag{1}$$

where A is the absolute area of the voltammogram cycle in coulombs (C), U is the potential window given by the difference between the upper limit (U_{max}) and lower limit (U_{min}) of the potential window in V, v is the scan rate in V s^{-1}, and $m_{\mathrm{electrode}}$ is the active mass of the electrode in grams. GCD analysis allows for the estimation of several values for evaluating the performance of ECCs: specific capacitance (C_{sp}), equivalent series resistance (ESR), specific energy density (E), specific power (P), and Coulombic efficiency (C_{eff} %) were calculated from Eqs. 2–6. The specific capacitance (C_{sp}) of the ECC cells (F g^{-1}) was estimated by means of Eq. 2:

$$C_{sp} = \frac{Q}{\Delta V_2 \times m_{\mathrm{electrode}}} = \frac{I \times t_{\mathrm{d}}}{\Delta V_2 \times m_{\mathrm{electrode}}} \tag{2}$$

where I is the current applied in A, t_{d} is the discharge time in seconds, ΔV_2 is the voltage range in which the discharge occurs, and $m_{\mathrm{electrode}}$ is the active mass of the electrode in grams. The ESR corresponds to the sum of all resistances of the electrochemical components in the ECC giving an *IR* drop in the charge/discharge cycles and can be estimated by Eq.3:

$$\mathrm{ESR} = \frac{\Delta V_1}{2 \times I} \tag{3}$$

where ΔV_1 is equal to the difference between the final potential recorded in the charge process and the first potential value recorded at the beginning of the discharge process, also known as the IR drop, and I is the current applied in A [23]. To evaluate the performance of the ECCs, specific energy density (W h kg^{-1}), specific power (W kg^{-1}), and Coulombic efficiency (C_{eff}%) were calculated by Eqs. 4–6 [24]:

$$E = \frac{C_{\mathrm{sp}} \times \Delta U^2}{2} = \frac{C_{\mathrm{sp}} \times (U_{\mathrm{max}} - U_{\mathrm{min}})^2}{2} \tag{4}$$

$$P = \frac{\Delta U}{4 \times \mathrm{ESR}} = \frac{(U_{\mathrm{max}} - U_{\mathrm{min}})}{4 \times \mathrm{ESR}} \tag{5}$$

$$C_{\mathrm{eff}} = \frac{t_{\mathrm{d}}}{t_{\mathrm{ch}}} \times 100 \tag{6}$$

Results and discussion

Morphology and structure

Morphology and structure of the carbonaceous support materials

Figure 1 shows the morphology and characterization of GO and rGO determined by SEM, XRD, and Raman spectroscopy analysis. Figure 1a, b shows SEM images of the carbonaceous supports. rGO exhibits expanded and separated flakes from the formation of CO and CO_2 gases in the thermal reduction process [25]. On the other hand, GO supports exhibit closely packed graphitic layers. From the XRD analysis, Fig. 1c shows the diffraction profiles of the GO and rGO carbonaceous supports. Both supports present the characteristic carbonaceous diffraction plane (002) located at around $2\theta = 25°$. Additionally, GO exhibits diffraction planes (001) and (004) located at $2\theta = 18°$ and 43°, respectively. These planes suggest a high graphitic orientation of the carbonaceous support [26]. These two diffraction planes are not present for rGO due to the thermal reduction process applied to the GO. The Raman spectra (Fig. 1d) show the graphitic active modes of GO and rGO in the range of 1300–1600 cm^{-1}. Modes D and G were observed in both materials with some differences. Active mode D (at 1356 cm^{-1}) is given by sp3 hybridization and its intensity is associated with the defects on the boundaries of graphitic flakes [27], while mode G (at 1590 cm^{-1}) corresponds to graphitic sp2 hybridization in the carbonaceous matrix [28]. GO showed a stronger D intensity associated with the defects on the surface induced by the chemical oxidation

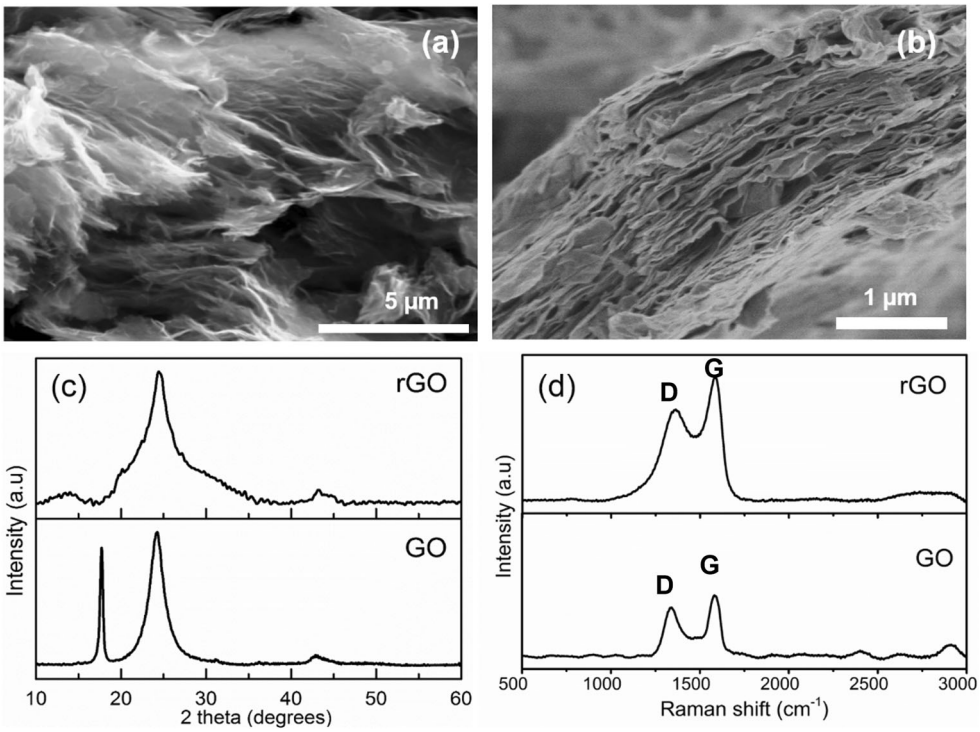

Fig. 1 SEM images of carbonaceous supports **a** rGO, **b** GO, **c** diffractograms for rGO and GO carbonaceous supports, **d** Raman spectra of rGO and GO carbonaceous supports

process. After thermal reduction of GO, the ratio between the normalized intensities quotient decreased from $I_D/I_G = 1$ for GO to $I_D/I_G = 0.73$, leading to the reduction of defects associated with oxygen functionalities on the edges of graphite oxide [29]. Thermal degradation of rGO was determined by TGA (Supplementary material, Fig. S3), with a residual mass of 6.9 % and a degradation temperature of 590 °C. Thermal degradation cannot be determined for GO due to the limiting thermal reduction process at 250 °C. The specific surface area of the carbonaceous supports was obtained through BET calculation, with specific surface area values of 28.44 and 332.8 $m^2\ g^{-1}$ for GO and rGO, respectively.

Morphology and structure of the composite materials

Figure 2 shows the structure and characterization of GO/Co_3O_4 and rGO/Co_3O_4 determined by SEM (Fig. 2a, b), XRD (Fig. 2c, d), Raman spectroscopy (Fig. 2e, f), and TGA (Supplementary info). The SEM images in Fig. 2a, b show well-dispersed microspheres of Co on the surface of both GO and rGO carbonaceous supports determined by EDS (Supplementary material, Fig. S1 and Table S1). The rGO/Co_3O_4-100 composite material (Fig. 2a) presented a packed structure different from the expanded layered rGO structure (Fig. 1a). The appearance of diffraction plane (001) at $2\theta = 18°$ is a characteristic of graphitized materials. The structural change of the support is due to the autogenous pressure during hydrothermal synthesis that causes a restacking of the graphitic sheets, as suggested by the SEM images (Figs. 1a and 2a). On the other hand, the GO support presents no structural change from the hydrothermal process, as suggested by the XRD diffractograms (Fig. 2d). The XRD patterns of the composite materials in Fig. 2c, d show distinctive Co_3O_4 phase signals according to JCPDS card 43-1003 with diffraction planes (111), (220), (311), (222), (400), and (511) located at $2\theta = 20°$, 31°, 37°, 39°, 44°, and 59°, respectively [16]. The lattice parameter was calculated by Rietveld refinement using FullProf © Suite 2.05 crystallographic software employing the reported space group Fd-3m (227) and showed a value of "a" = 8.078 Å for Co_3O_4. The lattice parameter "a" value obtained is slightly lower than that obtained by other Co_3O_4 preparation methodologies [30]. As the Co_3O_4 weight percent in the composite increases, the Co_3O_4 signal showed higher intensity over the carbonaceous (002) diffraction plane. Moreover, the samples with 10 and 100 wt% of Co showed a small contribution in the diffractograms corresponding to the non-reduced $Co(OH)_2$ formed by precipitation by the NaOH used as the pH mediator in the hydrothermal process. The diffraction peak agreed with JCPDS 74-1057 for plane (001) at $2\theta = 19°$ [31]. In the rGO/Co_3O_4 set of samples, the appearance of diffraction plane (001) in the composite materials suggests a change in the carbonaceous support structure due to autogenous pressure promoting a restacking of some of the graphitic sheets, as suggested by the SEM images (Figs. 1a and 2a). Raman spectroscopy showed that the active modes in the composite materials differed as the Co weight percent varied, with each Raman spectrum presenting two distinctive zones. The first zone located in the range between 471 and 680 cm^{-1} contains the active modes of Co_3O_4: active modes E_g, F_{2g}, and A_{1g} at 471, 515, and 680 cm^{-1}, respectively [32].

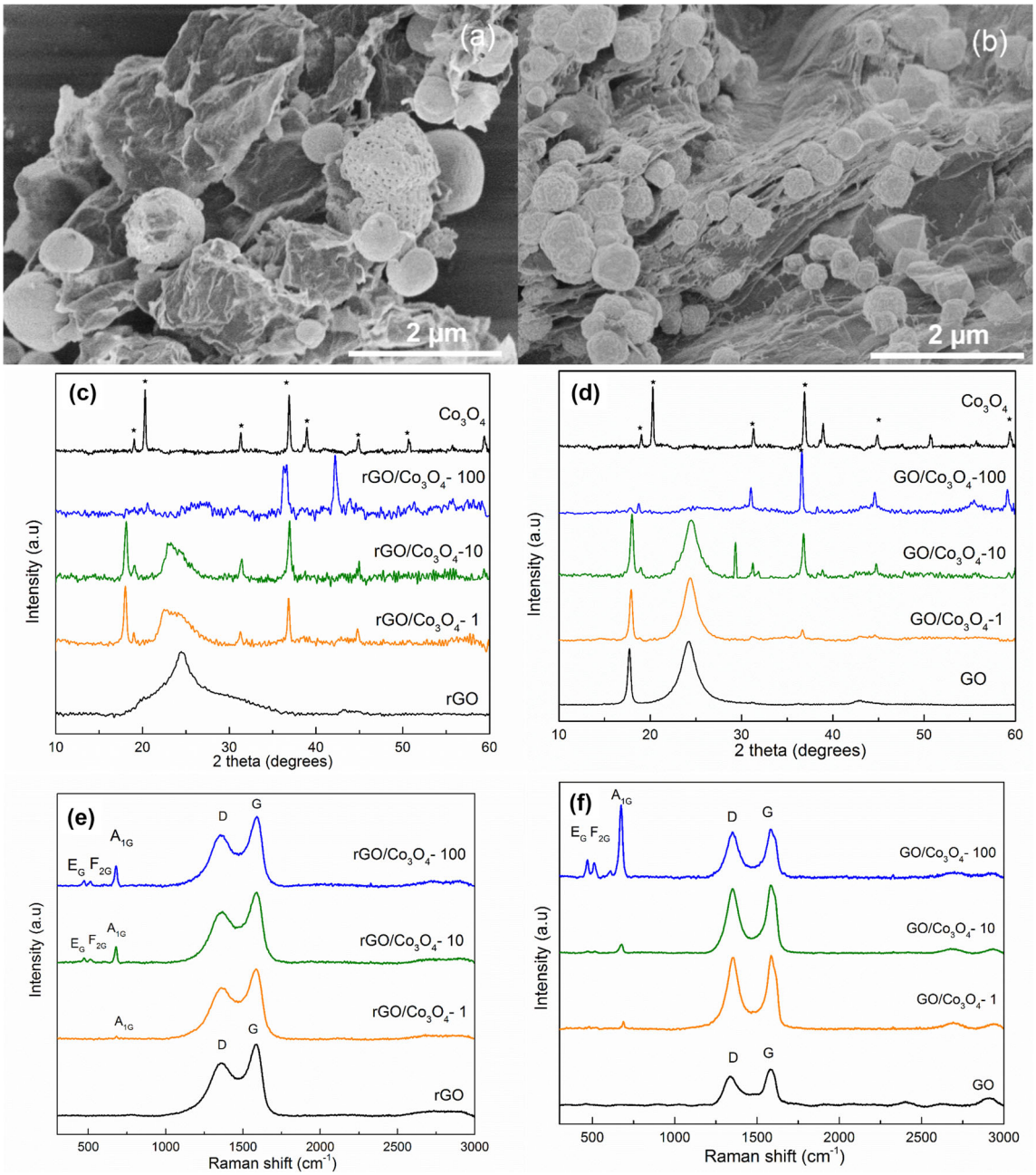

Fig. 2 SEM images of composite materials **a** rGO/Co_3O_4-100, **b** GO/Co_3O_4-100, **c** XRD pattern of GO/Co_3O_4-1, 10, and 100 composite materials, **d** XRD pattern of GO/Co_3O_4-1, 10, and 100 wt% composite materials, **e** Raman spectra of GO/Co_3O_4 composite materials, and **f** Raman spectra of rGO/Co_3O_4 composite materials

The second zone shows the graphitic signals of the GO and rGO carbonaceous supports. The GO/Co_3O_4-100 shows the strongest signal interaction between GO and Co_3O_4, indicated by the intensity of active mode A_{1g}. As the Co increased, the intensity of the active modes in Co_3O_4 decreased. Cobalt content was determined by TGA. The values obtained for the rGO/Co_3O_4 composite were 62.03, 11, and 1.86 % at the three different loadings of 100, 10, and 1 wt% with decomposition temperatures of 355, 360, and 370 °C, respectively. The measured values of Co in the GO/Co_3O_4 composites studied were 65.02, 14.26, and 3.28 % at the three different loadings of 100, 10, and 1 wt% with decomposition temperatures of 345, 350, and 370 °C. As such, the Co loading present in the samples accelerated thermal degradation by temperature ranges of 15 and 25 °C due to the decrease in the percentage of carbon in the composite materials [33]. The surface area of the GO-based composite materials increased with Co weight percent, with values of 51.10, 105.97, and 110.04 $m^2\ g^{-1}$ for GO/Co_3O_4 1, 10, and 100 wt%, respectively. This behavior can be attributed to the hydrothermal reduction of GO [8] and the

interaction of oxygen functionalities of GO with Co promoting different adsorption with the support. The rGO/Co_3O_4 composites presented a different behavior when Co weight percent increased. The specific surface area values reduced from 332.80 $m^2\ g^{-1}$ (rGO support) to 84.26, 76.24, and 57.49 $m^2\ g^{-1}$ for rGO/Co_3O_4 1, 10, and 100 wt%, respectively (Supplementary material Table S2).

Electrochemical characterization

Cyclic voltammetry analysis

Figures 3 and 4 show the evaluation through cyclic voltammetry of rate capability and electrochemical stability based on the capacitance response calculated by Eq. 1. The electrochemical behavior of the GO and rGO composite materials was evaluated at various scan rates of 1, 2, 5, 10, 20, 40, 60, 80, and 100 mV s^{-1}. Figure 3a shows the voltammogram for the ECC composed solely of the GO support. The low capacitance response and low electrochemical stability are attributed to the resistive behavior of GO caused by oxygen functional sites [34]. The square shape of the voltammogram characteristic of ECCs was maintained through all scan rates. The presence of a noticeable redox pair in GO/Co_3O_4-1 and 10 at potential values of 0.72 and 0.63 V for oxidation and reduction respectively improved the capacitance by Faradaic contribution. The redox pair in the GO/Co_3O_4-1 and 10 ECCs can be associated with an electrosorption process between oxygen functional sites in the GO promoting the nucleation of Co^{2+} ions and the progressive growth of Co_3O_4 microspheres. This phenomenon is caused by an electrodeficiency of solvated oxygen groups in GO and Co^{2+} ions in the hydrothermal synthesis process. The redox peaks can be associated with the reversible transition between Co_3O_4 and CoOOH, as shown in reaction 1 [35].

$$Co_3O_4 + OH^- + H_2O \leftrightarrows 3CoOOH + e^- \qquad \text{Reaction (1)}$$

The gradual incorporation of Co_3O_4 in GO showed an increase in capacitance with values of 485 and 376 F g^{-1} at 1 mV s^{-1} for GO/Co_3O_4-1 and Co_3O_4-10, respectively. As the scan rate increased, the GO-based ECCs showed high electrochemical stability with capacitance values of 224 and 205 F g^{-1} at the highest scan rate of 100 mV s^{-1}. When the Co_3O_4 loading reached a maximum value of 100 wt% (Fig. 3d), the ECC showed a notable decay in capacitance of 42 F g^{-1} at 100 mV s^{-1}. This decrease in capacitance can be associated with the coverage of Co_3O_4 on the GO support, thus limiting the capacitance response. Figure 4 shows the evaluation of rGO and rGO/Co_3O_4 ECCs by cyclic voltammetry. In contrast with GO, the rGO ECCs showed high capacitance values of up to 385 F g^{-1} when the Co_3O_4 loading reached a maximum value of 100 wt% (Fig. 4d) along with high scan rate capability as the square shape of the voltammogram was maintained through all scan rates ranging from 1 to 100 mV s^{-1}. Capacitive enhancement was observed with values of 705, 788, and 518 F g^{-1} at 1 mV s^{-1} for the rGO/Co_3O_4-1, 10, and 100 ECCs, respectively. As shown by the voltammogram, a low weight percent of Co_3O_4 (Fig. 4b) presented the highest capacitance values at low scan rates, but these values decreased rapidly down to 217 and 72 F g^{-1} for

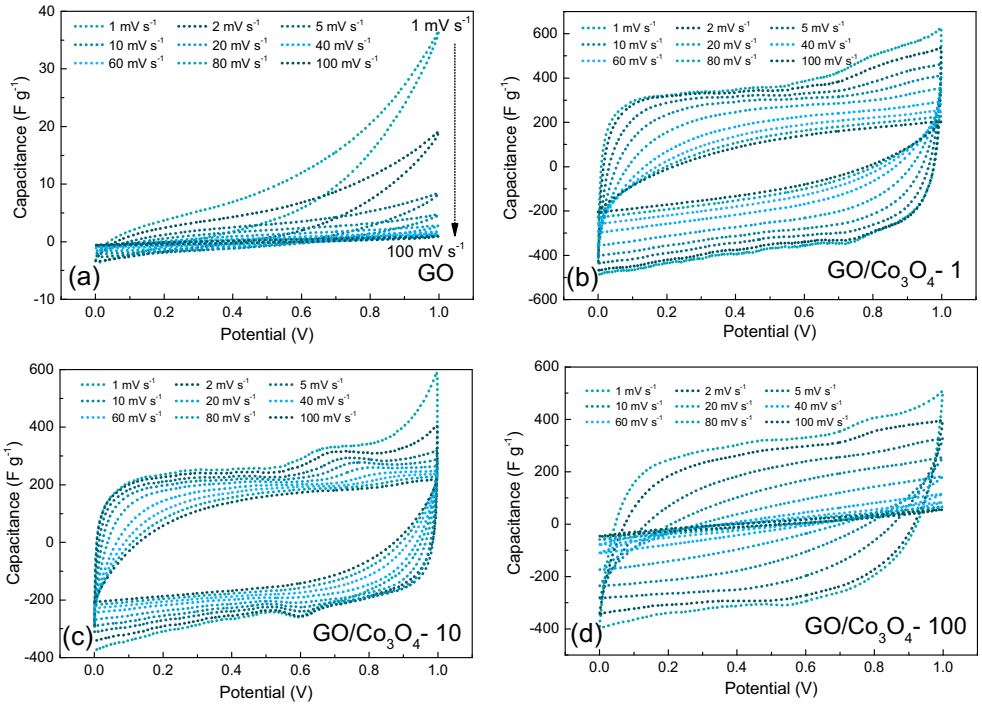

Fig. 3 Cyclic voltammograms for capacitance response **a** GO, **b** GO/Co_3O_4-1, **c** GO/Co_3O_4-10, and **d** GO/Co_3O_4-100 at various scan rates (1, 2, 5, 10, 20, 40, 60, 80, and 100 mV s^{-1})

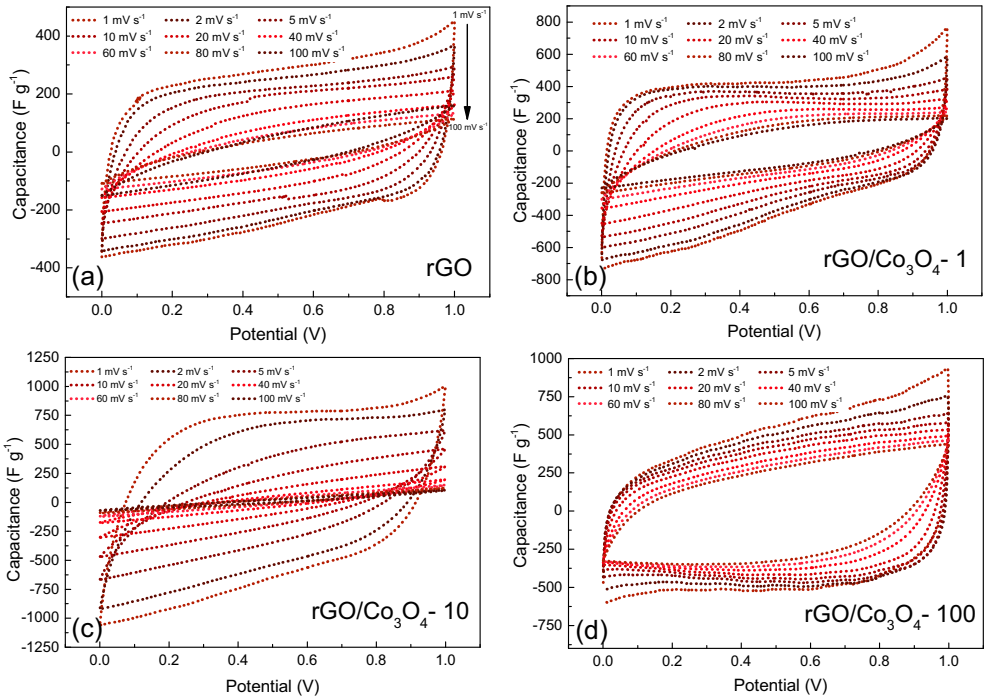

Fig. 4 Cyclic voltammograms for capacitance response **a** rGO, **b** rGO/Co_3O_4-1, **c** rGO/Co_3O_4-10 **d** rGO/Co_3O_4-100 ECCs at various scan rates (1, 2, 5, 10, 20, 40, 60, 80, and 100 mV s^{-1})

rGO/Co_3O_4-1 and 10 when the scan rate increased. The gradual incorporation of Co_3O_4 improved the rate capability (Fig. 4d), with the calculated capacitance decreasing by 36 % as the initial scan rate of 1 mV s^{-1} increased to 100 mV s^{-1}. The rate capability in ECCs is governed by the contributions of electrolyte diffusion, the adsorption of the charges at the electrode-electrolyte interface, and the charge transfer process in the bulk of the electrode [36]. Figure 5 compares the rate capability based on the calculated capacitance between the GO/Co_3O_4 and rGO/Co_3O_4 ECCs at the

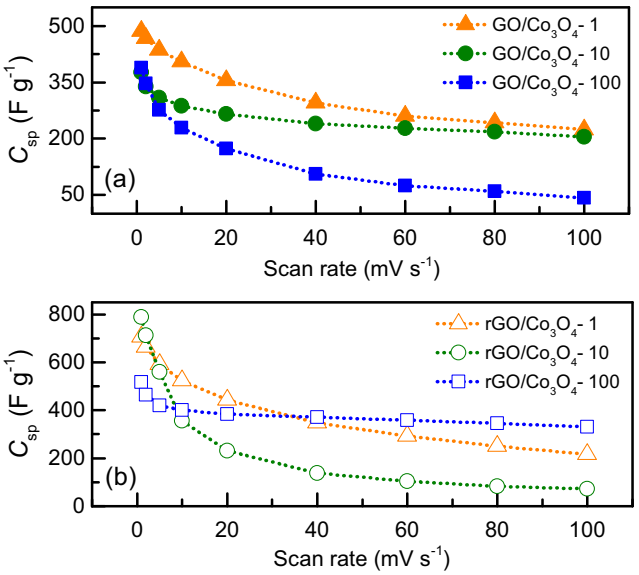

Fig. 5 Scan rate capability for **a** GO/Co_3O_4 1, 10, 100 wt% and **b** rGO/Co_3O_4 1, 10, 100 wt% ECCs, at various scan rates (1, 2, 5, 10, 20, 40, 60, 80, and 100 mV s^{-1})

scan rates evaluated. The integration of Co_3O_4 for both GO and rGO carbonaceous supports showed two different behaviors. For the GO/Co_3O_4 ECCs, the gradual increase in Co_3O_4 weight percent decreased the capacitance from 224 to 205 F g^{-1} and down to 42 F g^{-1} for GO/Co_3O_4-100. For the rGO/Co_3O_4 ECCs, the incorporation of high Co_3O_4 weight percent enhanced the scan rate capability and electrochemical stability, with the calculated capacitance being maintained with low variation throughout the entire scan rate range.

Evaluation of Co loading in composite material by galvanostatic charge/discharge cycling

Figure 6 shows the GCD profiles of the GO- and rGO-based composite material ECCs. Both the rGO- and GO-based ECCs exhibited a shape deviating from the triangular charge/discharge profile characteristic of ECCs. The deviation is attributed to the faradaic contribution of Co_3O_4. ESR calculated by Eq. 3 presents values of 0.113 Ω for rGO/Co_3O_4-100 and 0.172 Ω for GO/Co_3O_4-1 at 60 mA g^{-1}. These values suggest a minimal IR drop and good charge/discharge performance. As the charge density increased, the C_{sp} calculated by Eq. 2 decreased. GO/Co_3O_4-1 presented a maximum C_{sp} of 397 F g^{-1} at 60 mA g^{-1}, and this was reduced to 194 F g^{-1} when the charge/discharge rate increased to 1 A g^{-1}. For rGO/Co_3O_4-100, the increase in Co_3O_4 weight percent enhanced the C_{sp} with a maximum value of 452 F g^{-1} at 60 mA g^{-1} and it presented good C_{sp} retention when the current was increased to 1 A g^{-1}. This effect induced by Co_3O_4 weight percent also agrees with the CV profiles obtained for both ECCs with different carbonaceous supports. Figure 7a shows the charge

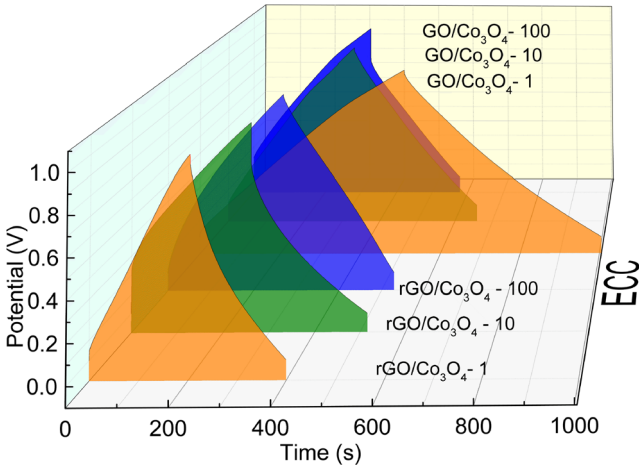

Fig. 6 Galvanostatic charge/discharge profile of GO and rGO composites with 100, 10, and 1 wt% Co_3O_4 at 0.06 A g^{-1}

density effect on C_{sp} at a charge/discharge rate between 0.03 and 1 A g^{-1}. C_{sp} decreased by 55 % for the GO-based ECCs, while the capacitance loss due to the charge density in rGO-based ECCs decreased 31 % for the rGO/Co_3O_4-100 ECC. The stability through the charge/discharge rates is associated with the low ESR given by the electronic conductivity of the rGO carbonaceous support. Figure 7b shows the efficiency of the ECCs (Eq. 6). The rGO/Co_3O_4-100 and GO/Co_3O_4-1 ECCs presented high C_{eff} values of 95 and 93 % respectively at the high charge/discharge current of 1 A g^{-1}. An activation process in the ECC is produced by the low charge/discharge current (30 mA g^{-1}) and occurs due to the low diffusion of the electrolyte in the bulk of the material showing high values of C_{eff} [37]. As current density increased together with the Co loading in the composite materials, the C_{eff} decreased due to a rapid charge transfer process. Figure 7c shows the Ragone plot for the given specific energy density (Eq. 4) and specific power (Eq. 5) for the GO- and rGO-based ECCs. GO-based ECCs showed an increase in the specific energy density as the Co_3O_4 weight percent increased with values of 34.54, 45.05, and 51.44 W kg^{-1} at 30 mA g^{-1}. Although, the energy density is proportional to Co_3O_4 weight percent in the ECCs, it decreased rapidly together with the charge/discharge rate to 26.59, 16.63, and 12.73 W kg^{-1} at 135 mA g^{-1} for the GO/Co_3O_4 1, 10, and 100 wt% ECCs, respectively. On the other hand, the Co_3O_4 weight percent in the ECCs is proportional to the specific power output, presenting values of 439.11, 439.52, and 800.85 W h kg^{-1} for the GO/Co_3O_4 1, 10, and 100 wt% ECCs respectively at 135 mA g^{-1}. The contribution of Co_3O_4 weight percent is given by the increase in surface area along the GO-based ECC materials (Table S2 Supplementary material). rGO-based ECCs showed an increase in specific energy density as the Co_3O_4 weight percent increased, with values of 27.18, 28.87, and 33.38 W kg^{-1} at 30 mA g^{-1}, decreasing to 8.58, 11.64, and 22.88 W kg^{-1} at 1 A g^{-1} for the rGO/Co_3O_4 1, 10, and 100 wt% ECCs, respectively. Specific power increased to 23.41 kW h kg^{-1} at 1 A g^{-1} for the rGO/Co_3O_4-1 ECC. In terms of overall performance, the rGO-based ECCs showed higher specific power output

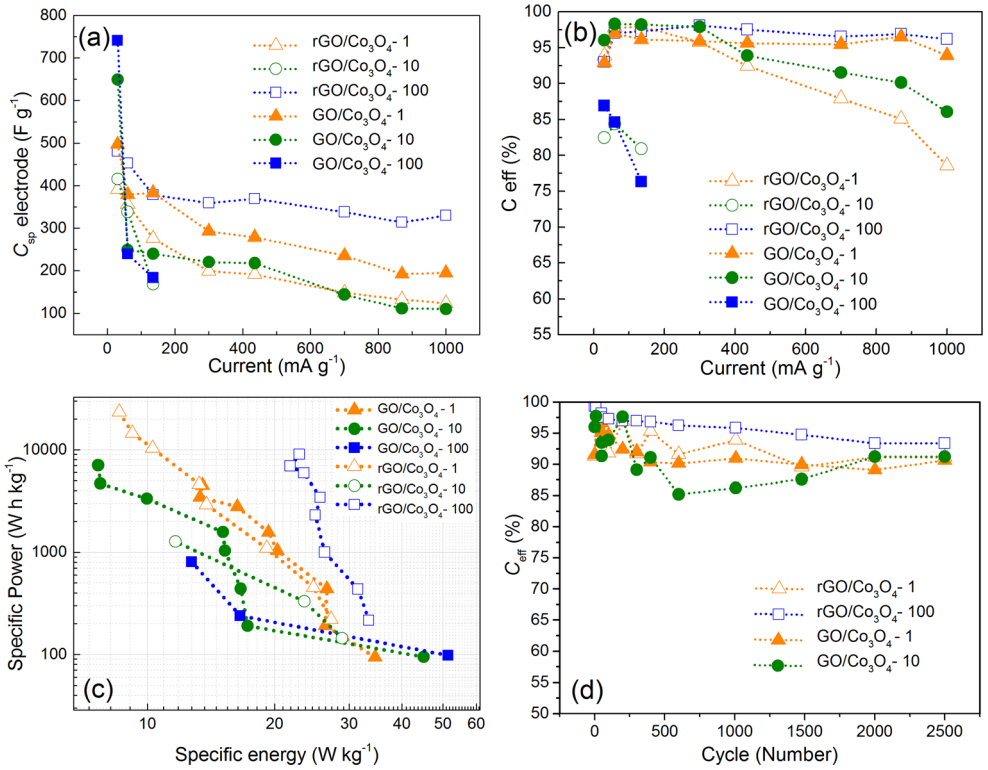

Fig. 7 Summarized data from galvanostatic charge/discharge cycling. **a** Calculated specific capacitances at different charge and discharge currents at different charge current densities (0.030, 0.06, 0.135, 0.300, 0.435, 0.700, 0.800, and 1 A g^{-1}). **b** C_{eff} determination of the ECCs. **c** Ragone plot distribution for evaluated ECCs. **d** Cyclability test for GO/Co_3O_4-1, rGO/Co_3O_4-1,GO/Co_3O_4-10, and rGO/Co_3O_4-100 ECCs for 2500 charge/discharge cycles at a charge current density of 0.030 A g^{-1}

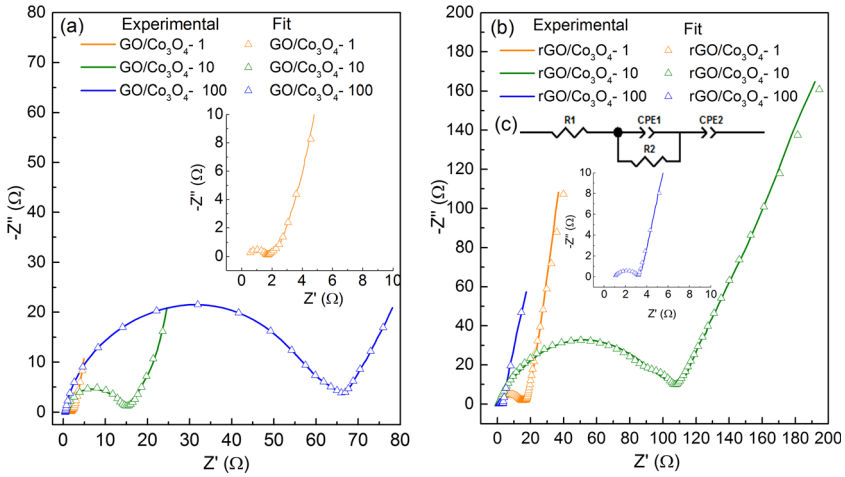

Fig. 8 Nyquist diagrams. **a** GO/Co_3O_4 ECCs (the *line* represents the experimental data and the symbol represents the fitted data from the proposed equivalent circuit, *inset*). **b** rGO/Co_3O_4 ECCs. **c** Proposed equivalent circuit diagram for the GO/Co_3O_4 1, 10, 100 wt% and rGO/Co_3O_4 1, 10, 100 wt% ECCs

than the GO-based ECCs as the charge/discharge rate increased. Figure 7d presents cyclability performance through 2500 galvanostatic charge/discharge cycles at 30 mA g^{-1} within a working voltage window from 0 to 1 V. The GO/Co_3O_4-1, rGO/Co_3O_4-1, GO/Co_3O_4-10, and rGO/Co_3O_4-100 ECCs were evaluated. The ECCs evaluated maintained a capacitance retention of 85 %, which demonstrates the good cycling stability of the composite as an active material with no significant loss retention. The number of cycles analyzed exceeded the average battery life cycle. The different behaviors can be explained as follows: the larger area of the rGO support offers more sites for the growth of Co microspheres in comparison with GO with a low specific area, although the presence of functional sites by chemically oxidized GO enhances the energy density, possibly by the electrosorption of Co^{2+} ions creating an in situ reduction of Co_3O_4 microspheres in the carbonaceous supports. These results are encouraging for the use of low area functionalized carbonaceous supports (GO), given that low specific surface materials by themselves do not represent a viable option in terms of electrochemical performance for ECCs, as suggested by the electrochemical characterization by cyclic voltammetry. However, the electrochemical performance was improved through the synthesis of a composite material by introducing a metal oxide material. The galvanostatic charge/discharge analysis indicated that the addition of Co_3O_4 offers an interesting insight, with the GO/Co_3O_4 1 ECC exhibiting 38 % less C_{sp} compared with the rGO/Co_3O_4 100 ECC. Based on this finding, two approaches are suggested: (1) the utilization of functionalized GO with a low area and rGO with a large area and no chemical functional sites for higher energy densities and (2) the use of rGO for high power output applications.

Electrochemical impedance spectroscopy analysis

Figure 8 shows the Nyquist diagrams for the GO/Co_3O_4 (Fig. 8a) and rGO/Co_3O_4 ECCs (Fig. 8b) and the proposed equivalent circuit (Fig. 8c). The electrochemical impedance spectroscopy analysis was carried out at equilibrium at 0 V vs. OCP with a signal amplitude of 10 mV for the composite ECCs. The proposed equivalent circuit is composed of three elements: an electrolytic resistance provided by R_1; followed by a series subcircuit in a parallel arrangement composed of a constant phase element CPE_1 and a second resistor R_2; which corresponds to the impedance arc in the kHz to Hz frequency range; followed by a second, series-connected CPE_2 in the low-frequency zone (<1 Hz), which represents the diffusion effects in the bulk of the composite materials. Fitting results obtained with Zview® software are shown in Table 1. The equivalent circuit component values present good fitting of the experimental data to the proposed equivalent circuit (Fig. 8c) with χ^2 values between 2 10^{-3} and 6 10^{-3}. The

Table 1 Summarized equivalent circuit component values for the PEIS analysis of the ECCs at 0 V vs. OCV in the frequency range from 300 kHz to 0.01 Hz

ECC	R_1 (Ω)	CPE_1-T (μF)	CPE_1-P (α)	R_2 (Ω)	CPE_2-T (mF)	CPE_2-P (α)	χ^2
GO/Co_3O_4–1	0.40	137.2	0.81	1.21	900	0.85	2.23 10^{-3}
GO/Co_3O_4–10	0.33	308.6	0.72	15.63	347	0.81	6.57 10^{-3}
GO/Co_3O_4–100	0.49	709.0	0.84	60.54	153	0.55	6.86 10^{-3}
rGO/Co_3O_4–1	0.41	204.3	0.73	15.90	86	0.85	4.23 10^{-3}
rGO/Co_3O_4–10	0.55	179.6	0.74	102.10	73	0.65	3.78 10^{-3}
rGO/Co_3O_4–100	0.98	845.0	0.62	2.28	147	0.85	2.20 10^{-3}

Ohmic electrolyte resistance agrees with the *ESR* values calculated by galvanostatic charge/discharge in both sets of ECCs. CPE_1-T values are in the order of microfarads and higher than 200 μF, corresponding to pseudocapacitance given by both storage mechanisms (ECDL and Faradaic contributions) [38], except for the GO/Co_3O_4–1 ECC, which may suggest that ECDL is the major storage mechanism. CPE-T is associated with the charge accumulated at the electrode-electrolyte interface [39]. The phase angle CPE_1-P indicates non-ideal capacitive behavior with values around $\alpha = 0.8$ [40]. R_2 is attributed to the charge transfer resistance processes in the ECCs, showing values up to 60.54 Ω for the GO/Co_3O_4–100 ECC. The increase in resistance is caused by the low electrical conductivity of Co_3O_4 coupled with the GO support. In the low-frequency region the second CPE_2 is associated with electrolyte diffusion in the bulk of the composite materials [41]. CPE_2-P showed higher values than CPE_1-P ($\alpha = 0.851$). The transfer component CPE_2-T is related to the capacitance in the bulk of the material [42], showing values of up to 900 mF, and this is associated with the specific surface area of the rGO-based composite and the Faradaic contribution from the metal oxide [43]. For the GO-based ECCs, a low weight percent of metal oxide enhanced the electrochemical behavior and for the rGO-based ECC a high weight percent of Co_3O_4 enhanced performance. Their behaviors agree with the electrochemical characterization by cyclic voltammetry and galvanostatic charge/discharge.

Conclusions

Composite materials with different carbonaceous supports and different cobalt oxide loadings were successfully synthesized through a facile hydrothermal process. The EECs based on the composite materials showed an excellent rate capability according to the CV analysis and stable electrochemical behavior. The rGO/Co_3O_4 ECCs presented better specific power output and better energy density behavior at the current densities evaluated up to 1 A g^{-1}. Meanwhile, the GO/Co_3O_4 EECs exhibited higher energy density values of 34, 45, and 51 W h kg^{-1} as the Co_3O_4 increased from 1 to 100 wt%, respectively. This result offers an insight into the different mechanisms by which metal oxides grow at different carbonaceous supports, with oxygen functional sites in the case of the GO and with a large specific area in the case of rGO, and how these characteristics present different behaviors when evaluated as ECCs.

Acknowledgments This work was supported by the Consejo Nacional de Ciencia y Tecnología (Mexico) CB 2011-166356 project fund. The authors would like to thank PRODEP for the support provided throughout the UQROO/DGIP/003/16 project; Consejo Nacional de Ciencia y Tecnología student grant (362308), and the CICY student exchange program. V.P., also acknowledges the technical support for characterization from M. Bass-López (CICY), I. Muñoz, J. Gómez, P. González, and E. Benito (ICTP).

References

1. Pandolfo AG, Hollenkamp AF (2006) Carbon properties and their role in supercapacitors. J Power Sources 157(1):11–27
2. Conway BE (1999) Electrochemical supercapacitors : scientific fundamentals and technological applications. Springer, New York
3. Ghosh A, Lee YH (2012) Carbon-based electrochemical capacitors. ChemSusChem 5(3):480–499
4. Wang FX, Xiao SY, Hou YY, Hu CL, Liu LL, Wu YP (2013) Electrode materials for aqueous asymmetric supercapacitors. RSC Adv 3(32):13059–13084
5. Jeong GH, Baek S, Lee S, Kim SW (2016) Metal oxide/graphene composites for supercapacitive electrode materials. Chemistry-an Asian Journal 11(7):949–964
6. Xin Zhaoa HT, Zhub M (2009) Carbon nanosheets as the electrode material in supercapacitors. J Power Sources 194:1208–1212
7. Wang Y, Shi Z, Huang Y, Ma Y, Wang C, Chen M (2009) Supercapacitor devices based on graphene materials. J Phys Chem C 113(30):13103–13107
8. Thi Toan N, Van Hoa N, Deivasigamani RK, Kharismadewi D, Iwai Y, Shim J-J (2016) Facile synthesis of cobalt oxide/reduced graphene oxide composites for electrochemical capacitor and sensor applications. Solid State Sci 53:71–77
9. Kumar N, Yu Y-C, Lu YH, Tseng TY (2016) Fabrication of carbon nanotube/cobalt oxide nanocomposites via electrophoretic deposition for supercapacitor electrodes. J Mater Sci 51(5):2320–2329
10. Zhou F, Liu Q, Gu J, Zhang W, Zhang D (2015) A facile low-temperature synthesis of highly distributed and size-tunable cobalt oxide nanoparticles anchored on activated carbon for supercapacitors. J Power Sources 273:945–953
11. Das B, Behm M, Lindbergh G, Reddy MV, Chowdari BVR (2015) High performance metal nitrides, MN (M = Cr, Co) nanoparticles for non-aqueous hybrid supercapacitors. Adv Powder Technol 26(3):783–788
12. Krishnan SG, Reddy MV, Harilal M, Vidyadharan B, Misnon II, Rahim MHA, Ismail J, Jose R (2015) Characterization of MgCo2O4 as an electrode for high performance supercapacitors. Electrochim Acta 161:312–321
13. Aravindan V, Reddy MV, Madhavi S, Mhaisalkar SG, Subba Rao GV, Chowdari BVR (2011) Hybrid supercapacitor with nano-TiP2O7 as intercalation electrode. J Power Sources 196(20): 8850–8854
14. Li Z-Y, Bui PTM, Kwak D-H, Akhtar MS, Yang OB (2016) Enhanced electrochemical activity of low temperature solution process synthesized Co3O4 nanoparticles for pseudo-supercapacitors applications. Ceram Int 42(1, Part B):1879–1885
15. Zhang C, Xie L, Song W, Wang J, Sun G, Li K (2013) Electrochemical performance of asymmetric supercapacitor based on Co3O4/AC materials. J Electroanal Chem 706:1–6
16. Wang XW, Liu SQ, Wang HY, Tu FY, Fang D, Li YH (2012) Facile and green synthesis of Co3O4 nanoplates/graphene nanosheets composite for supercapacitor. J Solid State Electrochem 16(11): 3593–3602
17. Dong C, Xiao X, Chen G, Guan H, Wang Y (2014) Hydrothermal synthesis of Co3O4 nanorods on nickel foil. Mater Lett 123:187–190
18. Hao Y, Wang H, Hu Z, Gan L, Xu Z (2015) Facile synthesis of mesoporous cobalt oxide rugby balls for electrochemical energy storage. New J Chem 39(1):68–71
19. Li Q, Hu X, Yang Q, Yan Z, Kang L, Lei Z, Yang Z, Liu Z (2014) Electrocapacitive performance of graphene/Co3O4 hybrid material prepared by a nanosheet assembly route. Electrochim Acta 119: 184–191
20. Bianco A, Cheng H-M, Enoki T, Gogotsi Y, Hurt RH, Koratkar N, Kyotani T, Monthioux M, Park CR, Tascon JMD, Zhang J (2013)

All in the graphene family—a recommended nomenclature for two-dimensional carbon materials. Carbon 65:1–6
21. Hummers WS, Offeman RE (1958) Preparation of graphitic oxide. J Am Chem Soc 80(6):1339–1339
22. Stoller MD, Park S, Zhu Y, An J, Ruoff RS (2008) Graphene-based ultracapacitors. Nano Lett 8(10):3498–3502
23. Subramanian V, Zhu H, Wei B (2006) Synthesis and electrochemical characterizations of amorphous manganese oxide and single walled carbon nanotube composites as supercapacitor electrode materials. Electrochem Commun 8(5):827–832
24. Kötz R, Carlen M (2000) Principles and applications of electrochemical capacitors. Electrochim Acta 45(15–16):2483–2498
25. Pei S, Cheng H-M (2012) The reduction of graphene oxide. Carbon 50(9):3210–3228
26. Dobiášová L, Starý V, Glogar P, Valvoda V (1999) Analysis of carbon fibers and carbon composites by asymmetric X-ray diffraction technique. Carbon 37(3):421–425
27. Kudin KN, Ozbas B, Schniepp HC, Prud'homme RK, Aksay IA, Car R (2008) Raman spectra of graphite oxide and functionalized graphene sheets. Nano Lett 8(1):36–41
28. Ferrari A, Meyer J, Scardaci V, Casiraghi C, Lazzeri M, Mauri F, Piscanec S, Jiang D, Novoselov K, Roth S, Geim A (2006) Raman spectrum of graphene and graphene layers. Phys Rev Lett 97: 187401
29. Chua CK, Sofer Z, Pumera M (2012) Graphite oxides: effects of permanganate and chlorate oxidants on the oxygen composition. Chem Eur J 18(42):13453–13459
30. Reddy MV, Beichen Z, Nicholette LJ, Kaimeng Z, Chowdari BVR (2011) Molten salt synthesis and its electrochemical characterization of Co3O4 for lithium batteries. Electrochem Solid-State Lett 14(5):A79–A82
31. Aghazadeh M, Barmi A-AM, Gharailou D, Peyrovi MH, Sabour B, Khosroshahi FN (2013) Cobalt hydroxide ultra-fine nanoparticles with excellent energy storage ability. Appl Surf Sci 283(0):871–875
32. Hadjiev VG, Iliev MN, Vergilov IV (1988) The Raman spectra of Co3O4. J Phys C Solid State Phys 21(7):L199
33. Blazsó M, Jakab E (1999) Effect of metals, metal oxides, and carboxylates on the thermal decomposition processes of poly (vinyl chloride). J Anal Appl Pyrolysis 49(1–2):125–143
34. Dreyer DR, Park S, Bielawski CW, Ruoff RS (2010) The chemistry of graphene oxide. Chem Soc Rev 39(1):228–240
35. Dong X-C, Xu H, Wang X-W, Huang Y-X, Chan-Park MB, Zhang H, Wang L-H, Huang W, Chen P (2012) 3D graphene–cobalt oxide electrode for high-performance supercapacitor and enzymeless glucose detection. ACS Nano 6(4):3206–3213
36. Li J, Zhao W, Huang F, Manivannan A, Wu N (2011) Single-crystalline Ni(OH)2 and NiO nanoplatelet arrays as supercapacitor electrodes. Nanoscale 3(12):5103–5109
37. García-Gómez A, Duarte RG, Eugénio S, Silva TM, Carmezim MJ, Montemor MF (2015) Fabrication of electrochemically reduced graphene oxide/cobalt oxide composite for charge storage electrodes. J Electroanal Chem 755:151–157
38. Conway BE, Pell WG (2003) Double-layer and pseudocapacitance types of electrochemical capacitors and their applications to the development of hybrid devices. J Solid State Electrochem 7(9): 637–644
39. Prabaharan SRS, Vimala R, Zainal Z (2006) Nanostructured mesoporous carbon as electrodes for supercapacitors. J Power Sources 161(1):730–736
40. Pacheco D, Smith M, Morales E (2011) Characterization of composite mesoporous carbon/conducting polymer electrodes prepared by chemical oxidation of gas-phase absorbed monomer for electrochemical capacitors. Int J Electrochem Sci 6(1):78–90
41. Li Y, Huang K, Liu S, Yao Z, Zhuang S (2011) Meso-macroporous Co3O4 electrode prepared by polystyrene spheres and carbowax templates for supercapacitors. J Solid State Electrochem 15(3): 587–592
42. Reddy MV, Prithvi G, Loh KP, Chowdari BVR (2014) Li storage and impedance spectroscopy studies on Co3O4, CoO, and CoN for Li-ion batteries. ACS Appl Mater Interfaces 6(1):680–690
43. Di Fabio A, Giorgi A, Mastragostino M, Soavi F (2001) Carbon-poly(3-methylthiophene) hybrid supercapacitors. J Electrochem Soc 148(8):A845–A850